Journal of Materials Chemistry B

ROYAL SOCIETY OF CHEMISTRY

PAPER

View Article Online
View Journal | View Issue

Cite this: J. Mater. Chem. B, 2023, 11, 6393

Nanozyme-based guanidinium peptides mediate surface reactive oxygen species for multidrug resistant bacterial infection management†

Xufeng Zhu,‡[ab] Qiang Sun,‡[abc] Jinjun Chen,[abc] Chunmei Liang,[abc] Liang Chen,[ab] Yi Qi,[ab] Hui Luo,[ab] Lanmei Chen*[c] and Jincan Chen *[abc]

Received 15th May 2023,
Accepted 31st May 2023

DOI: 10.1039/d3tb01104f

rsc.li/materials-b

Nanozymes are effective novel antibacterial agents. However, they still have some shortcomings such as low catalytic efficiency, poor specificity, and non-negligible toxic side effects. Here, we synthesized iridium oxide nanozymes (IrO_x NPs) by a one-pot hydrothermal method and used guanidinium peptide-betaine (SNLP/BS-12) to modify the surface of IrO_x NPs (SBI NPs) to obtain a high-efficiency and low-toxicity antibacterial agent. *In vitro* experiments showed that SBI NPs with SNLP/BS12 could enhance IrO_x NPs to target bacteria, mediate bacterial surface catalysis and reduce the cytotoxicity of IrO_x NPs to mammalian cells. Importantly, SBI NPs were able to effectively alleviate MRSA acute lung infection and effectively promote diabetic wound healing. Accordingly, iridium oxide nanozymes functionalized with guanidinium peptides are expected to be an effective antibiotic candidate in the postantibiotic era.

1. Introduction

Bacterial infections are a serious threat to human life and health, including chronic wound infection, chronic pneumonia, septicemia, endocarditis and so on.[1–3] At present, about 700 000 people die from bacterial infections every year. According to the World Health Organization's prediction, about 10 million people will die from bacterial infections in 2050, which is the total number of deaths from all diseases at present.[4–6] It can be seen that the diagnosis and treatment of bacterial infection is of great practical significance. The reasons for such high mortality rates due to bacterial infection are, on the one hand, the reduced retention of antibiotics by osmosis in the bacterial microenvironment and the up-regulation of the efflux pump for the excretion of foreign substances.[7–10] On the other hand, bacteria also acquire drug resistance through enzymatic degradation of antibiotics or changes in target proteins.[11–14] These factors directly increase the resistance of bacteria to traditional antibiotics. In addition, bacterial biofilms provide further protection for bacteria by establishing a resistant microenvironment that repels the penetration and retention of antibiotics.[15–20] Therefore, there is an urgent need to develop alternative antimicrobial therapies.

Bacterial surface modification technology has developed into an essential method for the diagnosis and treatment of bacterial infections.[21,22] For example, polypeptides or quaternary ammonium salts show a strong destructive effect on the surface structure of bacteria by modifying or combining with the surface.[23,24] Generally, the surface of bacteria is negatively charged, so the design of many polypeptide antibacterial agents focuses on the optimization of surface electrical properties.[25–27] For example, Professor Ji's group designed and constructed an antimicrobial agent with bacterial adaptive size and surface charge, which can enhance the effectiveness of anti-biofilm activity and the treatment of chronic lung infection.[16] It is worth noting that the previous work on peptide antibacterial materials mainly focused on the optimization and improvement of natural host defense polypeptides to enhance stability and antibacterial activity.[28,29] However, polypeptides are easily degraded by proteases in the body.[30] Therefore, Wang *et al.* designed a multi-armed guanidine-rich copolypeptide and realized the disturbance and destruction of the bacterial surface structure.[31] In addition, quaternary ammonium salt antibacterial agents are mainly bound to the surface of bacteria through electrostatic interaction, so as to achieve the purpose of destroying their surface structures.[26,32] Therefore, the technology based on bacterial surface modification is expected to enhance bacterial adhesion and destruction, and has significance for revealing nanomaterial functions and structures.

[a] The Marine Biomedical Research Institute, Guangdong Medical University, Zhanjiang, Guangdong, 524023, China. E-mail: jincanchen@126.com
[b] The Marine Biomedical Research Institute of Guangdong Zhanjiang, Zhanjiang, Guangdong, 524023, China
[c] Guangdong Key Laboratory for Research and Development of Natural Drugs, School of Pharmacy, Guangdong Medical University, Zhanjiang, Guangdong, 524023, China. E-mail: lanmeichen@126.com

† Electronic supplementary information (ESI) available. See DOI: https://doi.org/10.1039/d3tb01104f

‡ Both authors contributed equally to this work.

Sipunculus nudus Linnaeus peptide (SNLP) is a tripeptide derived from the marine source of *Sipunculus nudus*. The SNLP molecule contains a guanidine group that may have a strong affinity for gram-positive bacteria rich in negatively charged components. Moreover, Sangtanoo *et al.* found that the SNLP inhibited lipopolysaccharide-induced nitric oxide production by macrophages and had anti-inflammatory activity.[33] Lauryl betaine (BS-12) is a long chain alkyl quaternary ammonium salt, the long chain alkane allowing the molecule to be inserted into the bacterial wall membrane and significantly enhancing the antibacterial properties. In addition, the quaternary ammonium group is considered to be an effective antibacterial moiety. On this basis, Wu *et al.* combined BS-12 with a fluorescent carbon dot by covalent bonding and the presence of a hydrophobic long-chain alkane and a positively charged quaternary ammonium group allowed the fluorescent carbon dot to selectively attach to gram-positive bacteria, achieving both bacterial and antibacterial differentiation.[34] Therefore, the application of the anti-inflammatory activity of SNLP and the bacterially adherent reagent BS-12 in the fight against bacterial infections may be surprisingly effective.

Nanozyme-catalyzed therapy has been successfully used in preclinical studies of many diseases and has shown promising clinical applications, especially in the eradication of biofilms and the treatment of bacterial infections.[35–40] A kind of nanomaterial with enzyme-like activity is called a nanozyme, which has the advantages of low cost, simple preparation, high stability and adjustable enzyme activity.[41,42] At present, many nanomaterials (Ag/CaP coatings, Ag nano flowers, Fe_3O_4 nanoparticles, EtNBSS NPs, UCNANs, and hydrogel) have been developed for the treatment of bacterial infections.[43–48] Generally, the biofilm microenvironment has the characteristics of low pH (4.5–6.5), high expression of enzymes (esterase, lipase, and hyaluronidase), high concentration of H_2O_2, hypoxia, *etc.*[49–51] It has been reported that nanozymes catalyze endogenous H_2O_2 in the infected microenvironment to generate high levels of $^{\bullet}OH$, thereby destroying the bacterial biofilm.[52] It is worth noting that a single ROS molecule is very short (possibly at the nanosecond level), easily decomposed into other oxidizing substances and has a small range of action (<200 nm).[53] To solve these problems, Yang's group and Xiong's team designed a series of silver palladium alloy (AgPd) nanocages, from which they selected those that could efficiently generate surface-bound ROS by *in situ* catalysis, thus realizing the antibacterial activity of nanozymes with high efficiency and low toxicity.[54] Therefore, the construction of nano-catalytic therapy with surface-bound ROS of bacteria can further improve the antibacterial effect.

In this work, we synthesized SNLP/BS-12 *via* a classical ester condensation reaction and then directly synthesized SNLP/BS-12@IrO_x NPs (SBI NPs) using a one-pot hydrothermal method. The prepared SBI NPs exhibited excellent POD-like activity, bacterial targeting and antibacterial activity. *In vivo* experiments demonstrated the potential of SBI NPs to treat acute lung infections and to promote diabetic wound healing (Scheme 1). This study demonstrates the potential of multifunctional nanozymes with bacterial targeting, pH-responsive catalytic production of

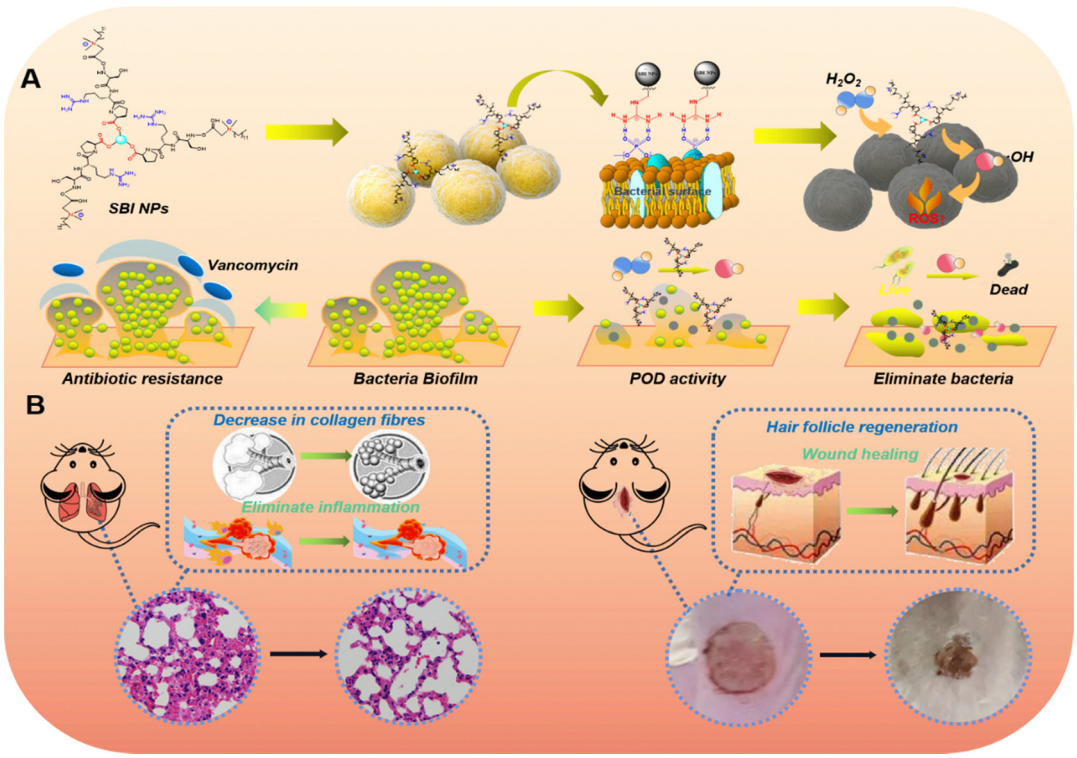

Scheme 1 Schematic illustration of guanidine-based peptide-functionalized nanozymes mediating bacterial surface enzyme catalysis, resistance to biofilms and anti-bacterial infection activity *in vivo*.

ROS and promotion of wound healing for practical clinical applications.

2. Results and discussion

Synthesis and characterization of SBI NPs

Iridium oxide nanoparticles (IrO_x NPs) have excellent enzymatic activity and stability, and have been widely used for cancer treatment and imaging diagnostic reagents.[55] Referring to the previous method,[55,56] we fabricated IrO_x NPs by the direct thermal hydrolysis method of $IrCl_3{\cdot}xH_2O$. Transmission electron microscopy (TEM) images showed that IrO_x NPs hold a typical spherical structure and the particle size is 30.9 ± 11.4 nm (Fig. 1A and Fig. S1, ESI†). In order to reduce the cytotoxicity of IrO_x NPs to normal mammalian cells and improve the antibacterial efficiency, marine peptides with a guanidine group (SNLP) and lauryl betaine (BS-12) were selected for surface modification of IrO_x NPs. Synthesis of SNLP/BS-12 was carried out using esterification condensation, and the NMR hydrogen spectrum (Fig. S2 and S3, ESI†) indicated that the two amino groups on one SNLP molecule would be replaced by BS-12 molecules, respectively. Afterwards, different mass ratios of SNLP/BS-12 and $IrCl_3{\cdot}xH_2O$ were reacted at 80 °C for 6 h using a one-pot hydrothermal method under alkaline conditions (the product was named SBI NPs). TEM images revealed that the SBI

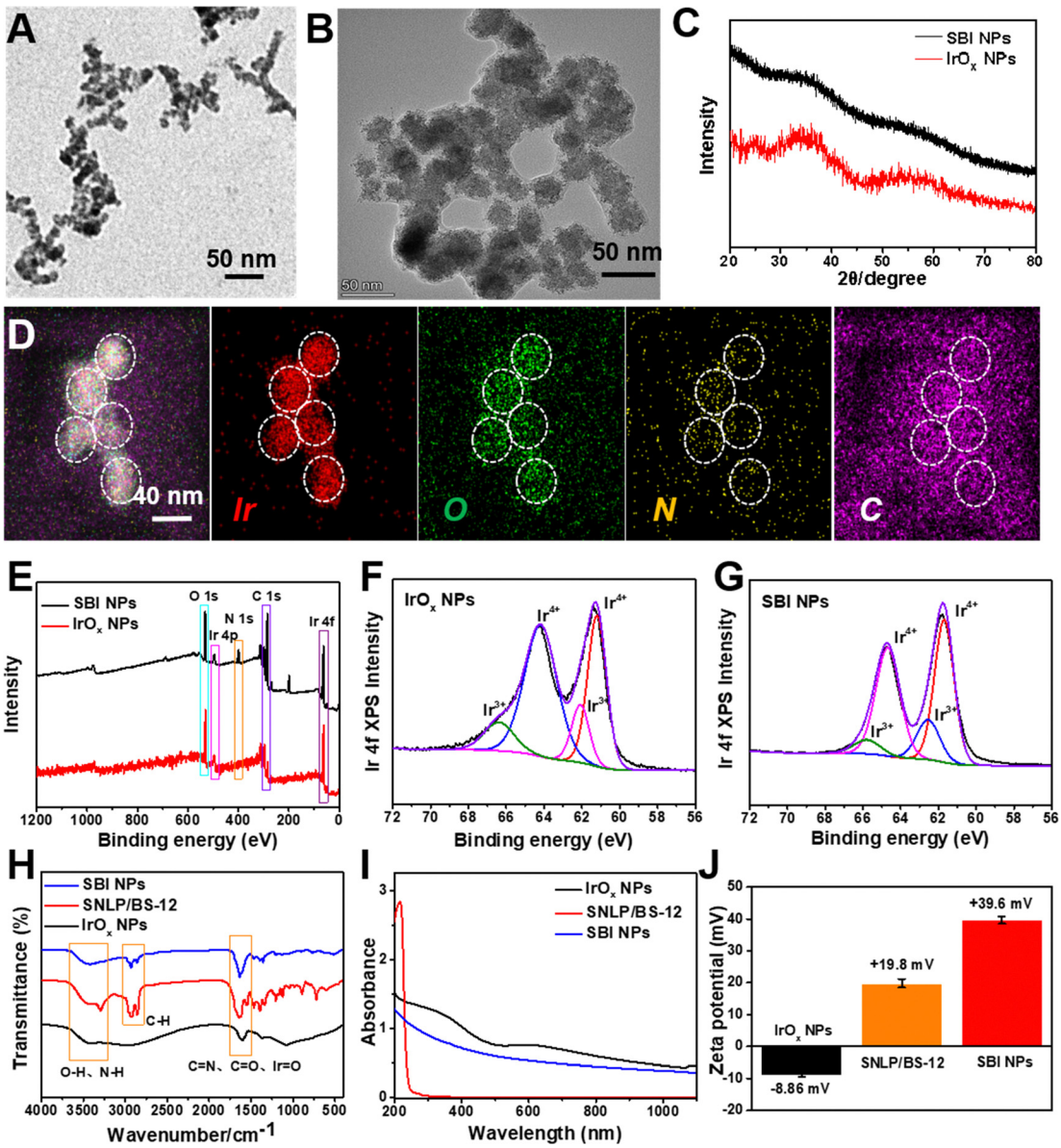

Fig. 1 Synthesis and characterization of SBI NPs. TEM images of (A) IrO_x NPs and (B) SBI NPs. (C) XRD of IrO_x NPs and SBI NPs. (D) HAADF-STEM image and EDX elemental mapping of SBI NPs (red: Ir; green: O; yellow: N; and purple: C). (E) XPS of IrO_x NPs and SBI NPs. (F) Ir 4f XPS spectra of the prepared (F) IrO_x NPs and (G) SBI NPs. (H) FT-IR spectra of IrO_x NPs, SNLP/BS-12 and SBI NPs. (I) UV-vis-NIR spectra of IrO_x NPs, SNLP/BS-12 and SBI NPs. (J) Zeta potentials of IrO_x NPs, SNLP/BS-12 and SBI NPs.

NPs also have a spherical morphology with a diameter of 36.9 ± 4.98 nm. (Fig. 1B and Fig. S4, ESI†). Since the small *granulums* are at the lower limit of X-ray powder diffraction (XRD), the XRD spectrum shows a very broad peak (Fig. 1C).[57] Energy-dispersive spectrometry (EDS) analysis of SBI NPs proves the presence of Ir, O, N, and O elements (Fig. 1D and Fig. S5, ESI†), which are distributed uniformly. X-Ray photoelectron spectroscopy (XPS) results (Fig. 1E) displayed that both IrO_x NPs and SBI NPs have C 1s, O 1s and Ir 4p peaks, and both of those Ir 4f peaks have similar peak shapes, while the difference between IrO_x NPs and SBI NPs is the presence of N 1s peaks as well as higher C 1s peaks in SBI NPs, indicating the successful synthesis of SBI NPs. The X-ray photoelectron spectroscopy (XPS) spectra of IrO_x NPs and SBI NPs in the Ir 4f region exhibited two binding peaks at around 61.76 and 64.71 eV, corresponding to Ir^{4+} at 61.67 and 64.69 eV, and Ir^{3+} at 62.55 and 65.81 eV, respectively (Fig. 1F–G). FT-IR spectra exhibited that the SBI NPs, SNLP/BS-12 and IrO_x NPs had very broad peaks at 3750–3250 cm^{-1}, indicating the presence of O–H, whereas SBI NPs and SNLP/BS-12 additionally have N–H bonds and showed higher peaks. Compared to IrO_x NPs, SBI NPs and SNLP/BS-12 revealed higher peaks at 3000–2700 cm^{-1} as well as 1690–1500 cm^{-1} due to the presence of C–H, C=N, C=O and Ir=O (Fig. 1H). UV-vis spectra (Fig. 1I) showed that SBI NPs and IrO_x NPs have a very broad absorption distribution at 190–1100 nm. In addition, zeta potential results revealed that IrO_x NPs, SNLP/BS-12 and SBI NPs have −8.86, +19.8 and 39.6 mV, respectively (Fig. 1J) and the positive potential of the SBI NPs may be attributed to the positive charge of SNLP/BS-12. The above data confirmed that SBI NPs have been successfully synthesized.

Catalytic performance of SBI NPs

It is an effective antibacterial strategy to use nanozymes to catalyze endogenous H_2O_2 and then produce highly toxic reactive oxygen species against MRSA infection.[58] Therefore, we investigated the catalytic activity of SBI NPs at different pH conditions and examined the type of reactive oxygen species. The peroxidase-like activity of SBI NPs was studied through the catalytic oxidation of 3,3′,5,5′-tetramethylbenzidine (TMB). In the presence of H_2O_2, the characteristic absorption peak of oxidized TMB at 652 nm is used as an indicator (Fig. 2A). As shown in Fig. 2B, IrO_x NPs with TMB and H_2O_2 have a distinct characteristic absorption peak at 652 nm. As the bacterial microenvironment is weakly acidic (pH 4.5–6.5), we studied the POD-like activity of the NPs under weakly acidic as well as physiological environmental conditions. As shown in Fig. 2C and D, IrO_x NPs and SBI NPs can catalyse the production of oxidative TMB in the presence of H_2O_2 in a pH-

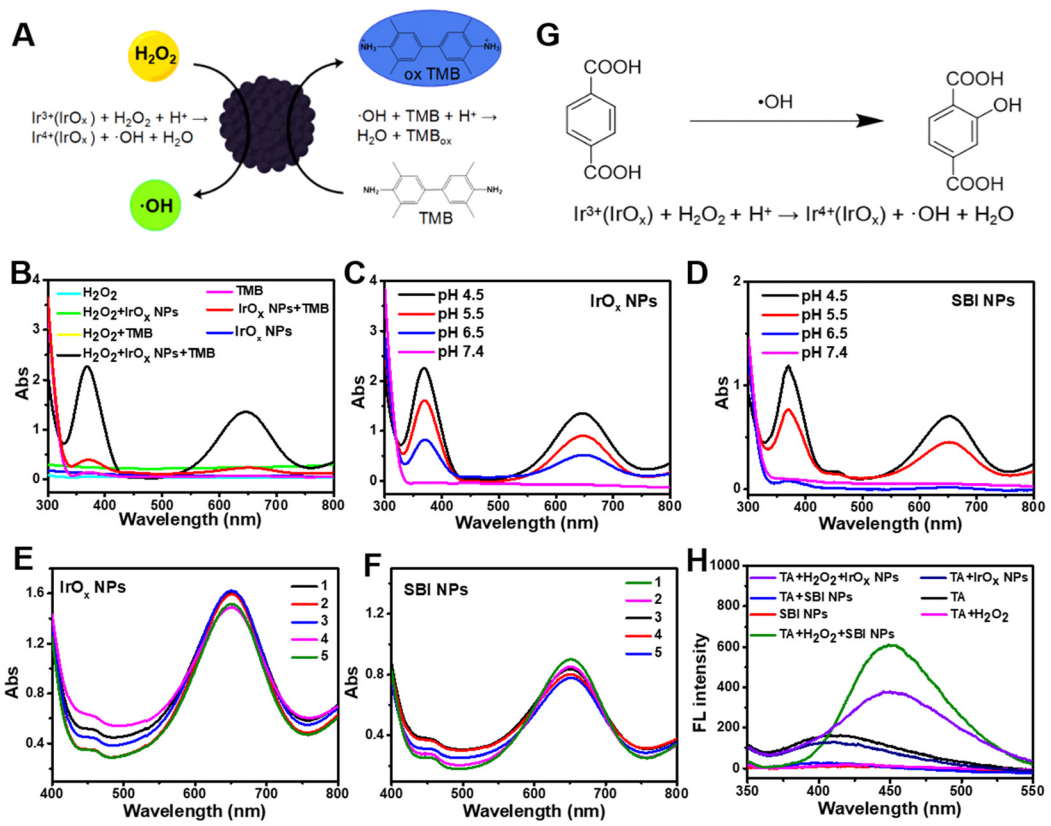

Fig. 2 Peroxidase activity of SBI NPs. (A) Schematic illustration of the mechanism of IrO_x NPs. (B) POD-like activities of IrO_x NPs with different agents. POD-like activities of (C) IrO_x NPs and (D) SBI NPs were evaluated under different pH conditions. Absorbance spectra of TMB with different cycles of (E) IrO_x NPs and (F) SBI NPs (HAc-NaAc buffers, pH = 4.5). (G) The principle of determination of •OH production by the TA method. (H) The measurement of •OH generation in different solutions using TA as a fluorescent indicator.

dependent manner and have almost no catalytic activity at pH 7.4, indicating indirectly the safety of SBI NPs under physiological conditions. The sustained catalytic capacity is also an important part of the evaluation of nanomaterials. As shown in Fig. 2E and F, the IrO_x NPs and SBI NPs remained stable in their catalytic capacity for five cycles of catalysis. Afterwards, we used terephthalic acid (TA) as an indicator to detect the OH generated by different components during catalytic oxidation under HAc–NaAc buffers at pH 4.5 (Fig. 2G). As shown in Fig. 2H, the TA fluorescence intensity of SBI NPs + H_2O_2 was much higher than those of the other groups, indicating that SBI NPs were able to effectively convert H_2O_2 to •OH. Next, we compared the POD activity of SBI NPs at different pHs as well as at different temperatures, which showed that the strongest activity was found under acidic conditions and tepid environments (Fig. S6 and S7, ESI†). The catalytic performance of SBI NPs was further investigated by the enzyme kinetics theory and typical enzymatic reaction kinetics was monitored within the specifed range of TMB or H_2O_2 concentrations. For catalytic reactions, the Michaelis–Menten constant (K_m) represents the affinity of the substrate and the enzyme and a lower K_m value indicates a higher affinity of the enzyme for the substrate. Based on the initial reaction rate and the double-reciprocal plot of the Lineweaver–Burk equation, the K_m of SBI NPs was determined to be 79.4×10^{-3} M with H_2O_2 as the substrate and the V_{max} was 153×10^{-8} M s^{-1} (Fig. S8, ESI†). The K_m was determined to be 95.82×10^{-6} M with TMB as the substrate, and the V_{max} was 126.4×10^{-8} M s^{-1} (Fig. S9, ESI†), indicating comparable affinity to that of nanomaterials (Table S1, ESI†).

Antibacterial activity of SBI NPs *in vitro*

We selected MRSA and *E. coli* as research objects and used growth curves to show the effects of different concentrations of IrO_x NPs on bacterial growth (Fig. S10, ESI†). It can be seen that the IrO_x NPs had the ability to inhibit the growth of MRSA, while it has almost no inhibitory activity against the negative bacterium *E. coli*. To enhance the anti-MRSA activity of IrO_x NPs, we loaded them with a reagent with a bacterial surface modification effect, SNLP/BS-12. Firstly, we explored whether the inhibition of MRSA by SNLP, BS-12 and SNLP/BS-12 with IrO_x NPs was synergistic, and the results showed that the fractional inhibitory concentration (FIC) indexes between them were 0.5, indicating that both of them have an additive relationship (Fig. S11, ESI†). After that, we evaluated the effect of SBI NPs synthesized with different feeding ratios of SNLP/BS-12 and $IrCl_3 \cdot xH_2O$ on bacterial activity. The results showed that the antibacterial activity of SBI NPs was the best when the feeding ratio was 1 : 1 (Fig. S12, ESI†). Based on the excellent ability of both NPs to inhibit bacterial growth, we evaluated the antibacterial performance of each component against MRSA using a colony-forming unit (CFU) assay and used vancomycin, a first-line anti-MRSA drug, as a positive control (Fig. 3A and B). As shown in Fig. S14 (ESI†), SBI NPs exhibited antibacterial activity and showed concentration dependence. Similarly, we compared

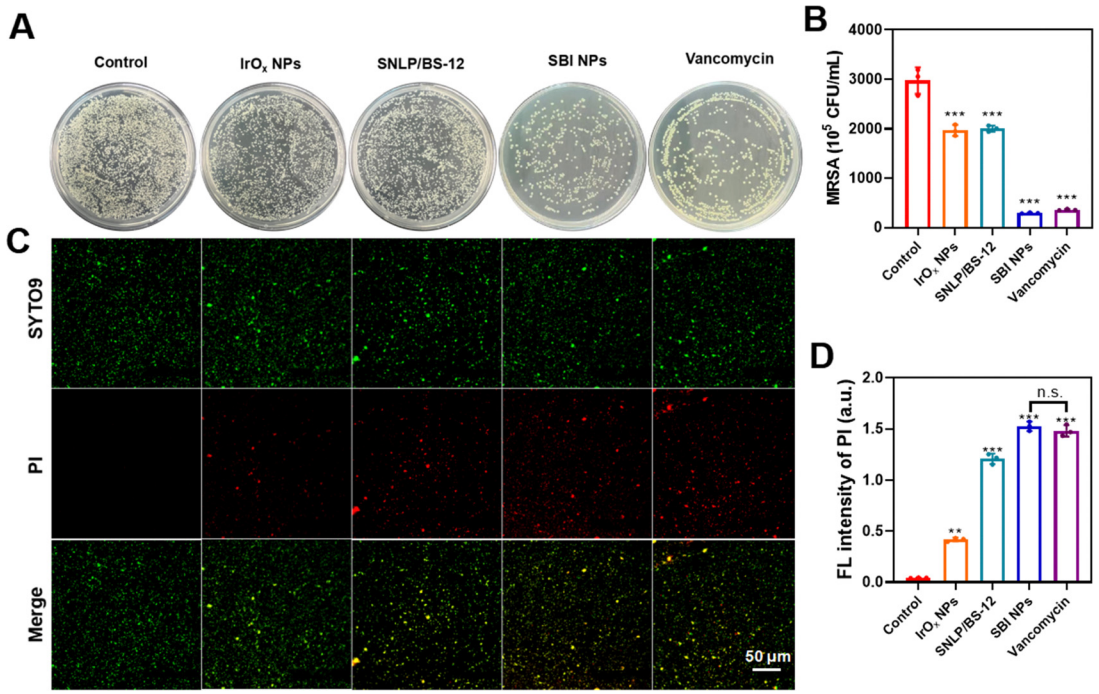

Fig. 3 Anti-bacterial activities of NPs *in vitro*. (A) Photographs of bacterial colonies formed by MRSA treated with different components. (B) Bacterial survival of MRSA by the plate counting approach. (C) Live/dead fluorescence staining images of MRSA using SYTO9/PI after various therapies. Scale bar: 50 μm. (D) PI fluorescence intensity using ImageJ software. The concentrations of IrO_x NPs, SNLP/BS-12, SBI NPs and vancomycin were 1/2 × MIC values and treated with PBS as a control group. The final concentration of MRSA was 5×10^5 CFU mL^{-1}. *$p < 0.05$; **$p < 0.01$; ***$p < 0.001$ and n.s. not significant.

the PI fluorescence intensity of SBI NPs after treatment of MRSA with each component, using the live/dead bacteria staining (Syto9/PI) method, which could be observed by confocal laser scanning microscopy (CLSM) and was comparable to that of the vancomycin group, indicating that SBI NPs had a significant ability to kill MRSA (Fig. 3C and D). We also evaluated the fluorescence intensity of MRSA after treatment with SBI NPs (Fig. S15, ESI†), and the PI fluorescence gradually increased with increasing concentrations of SBI NPs, indicating an increase in dead bacteria, which was consistent with the results of CFU. Compared to currently reported anti-bacterial nanozymes, SBI NPs have considerable activity (Tables S2 and S3, ESI†).

Antibiofilm activity of SBI NPs

It has been reported that ROS are capable of damaging the dense structure of bacterial biofilms (Fig. 4A).[59] To explore the anti-biofilm activity of SBI NPs, we constructed a biofilm formation inhibition assay by crystal violet staining (CV staining). As shown in Fig. 4B and C, after co-incubating the different treatment groups with MRSA for 24 h and 72 h, it was found that the SBI NP group almost completely inhibited biofilm formation, while IrO_x NPs required a longer incubation time (72 h) and were also only able to partially inhibit biofilm formation (Fig. 4D and E). Meanwhile, we performed 3D fluorescence imaging of MRSA biofilms (Fig. 4F) and the experimental results were consistent with those of CV staining. Subsequently, we performed similar experiments with different concentrations of SBI NPs, which, as seen in Fig. S15 (ESI†), have a strong ability to inhibit biofilm formation at low concentrations (31.25 μg mL^{-1}). These results indicated that SBI NPs have good anti-biofilm formation activity.

Anti-bacterial mechanism of SBI NPs

Based on the excellent anti-bacterial and anti-biofilm activities of iridium oxide nanoenzymes, we further investigated the anti-bacterial mechanism (Fig. 5A). Firstly, we evaluated the ability of SNLP/BS-12-mediated bacterial targeted labeling. Rho B-labeled SBI NPs (Rho B-SBI NPs) were used for co-incubation with MRSA. Using laser confocal microscopy, as we expected (Fig. 5B), Rho B-SBI NPs (red fluorescence) and MRSA (blue fluorescence) showed clear colocalization, indicating that SBI NPs were able to target MRSA. Subsequently, we incubated Rho B-labeled SNLP/BS-12 (Rho B-SNLP/BS-12) with MRSA (Fig. 5C) and Rho B-SBI NPs with HUVECs (Fig. 5D). The results confirmed that the binding of SBI NPs to MRSA was due to SNLP/BS-12. It is worth

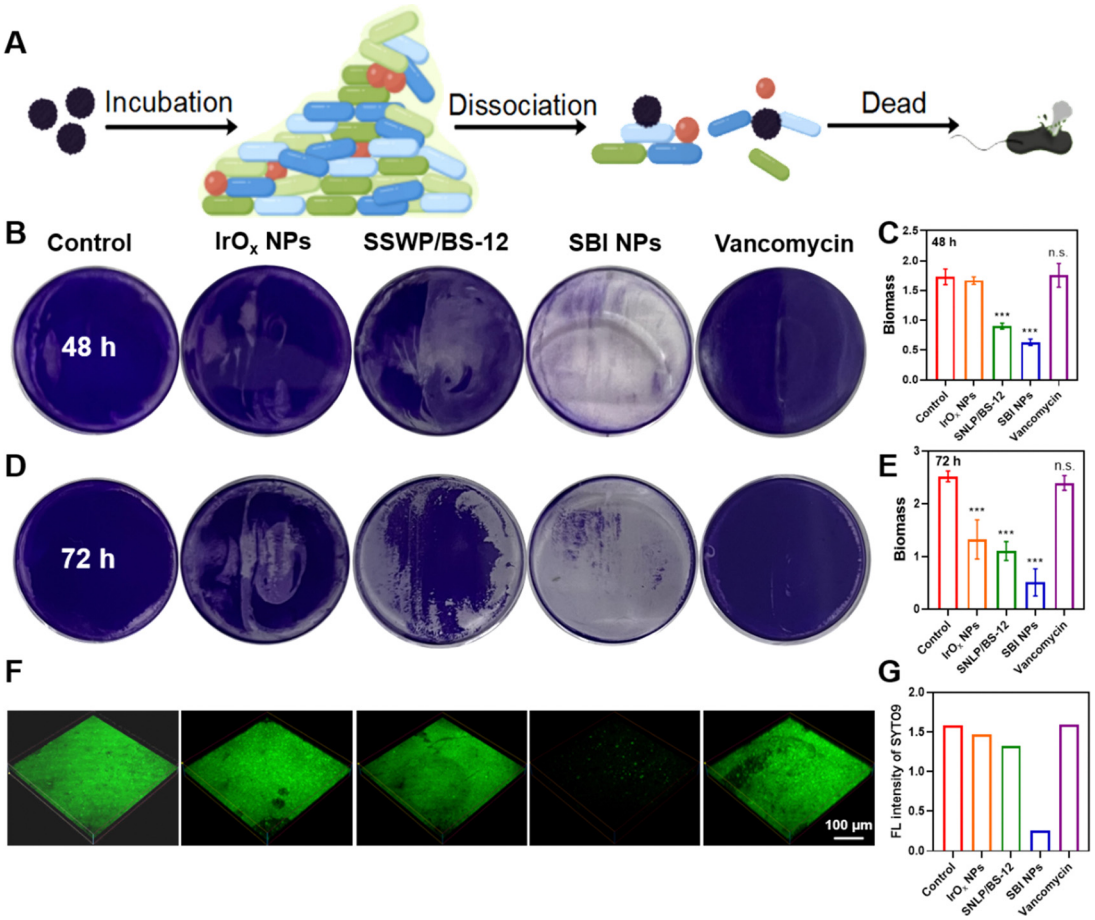

Fig. 4 Anti-biofilm properties of NPs. (A) Illustration of MRSA biofilm damaged by NPs. (B and D) CV staining results of inhibitory effects of different components on MRSA biofilm formation for 48 h and 72 h. (C and E) Biofilm biomass of MRSA biofilms corresponding to CV staining results. (F) 3D confocal fluorescence images of MRSA biofilms treated with various components for 24 h staining with SYTO9. Scale bar: 100 μm. (G) SYTO9 fluorescence intensity. *$p < 0.05$; **$p < 0.01$; ***$p < 0.001$ and n.s. not significant.

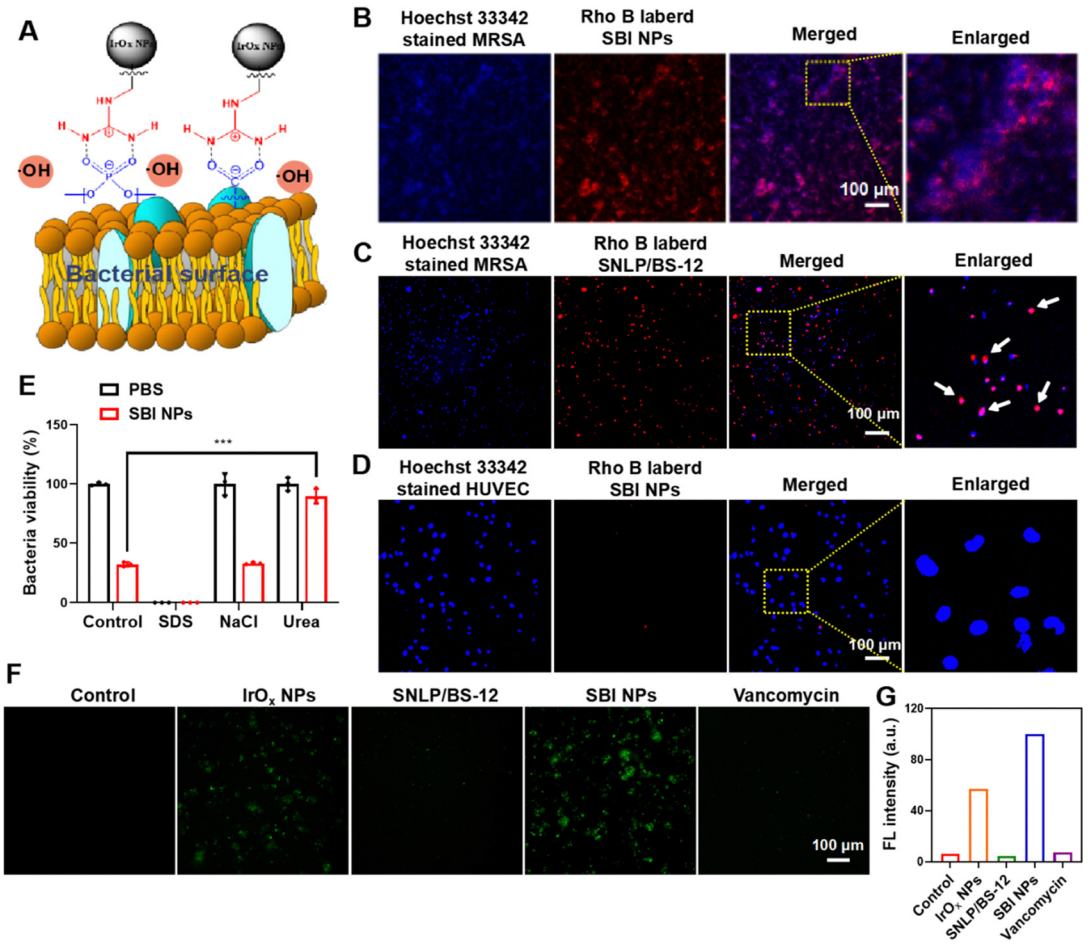

Fig. 5 Anti-bacterial mechanism of SBI NPs. (A) Mechanism diagram of SBI NPs and MRSA. (B) The binding of Rho B-SBI NPs and Hoechst 33342 labeled-MRSA was observed after co-incubation. (C) The binding of Rho B-SNLP/BS-12 and Hoechst 33342-labeled MRSA was observed after co-incubation. (D) The binding of Rho B-SBI NPs and Hoechst 33342-labeled HUVECs was observed after co-incubation. Scale: 100 μm. (E) Bacterial viability of MRSA treated with different components (PBS, 0.1% SDS, 0.5 M NaCl, and 50 mM urea) and after 24 h of addition of SBI NPs. The viability of bacteria with the addition of different components was set to 100%. (F) A DCFH-DA fluorescent probe was used to detect the changes in ROS content of MRSA treated with different components. (G) Quantification of fluorescence intensity. (Compared with the control group, $*p < 0.05$, $**p < 0.01$, $***p < 0.001$.)

noting that SBI NPs do not target and label normal HUVEC cells, indicating that SBI NPs have high-efficiency and low-toxicity antibacterial ability.

In addition, to further investigate the binding mode of SBI NPs to MRSA, we co-incubated SBI NPs and MRSA with NaCl (to separate electrostatic interactions), sodium dodecyl sulfate (SDS, to interrupt the formation of hydrophobic interactions), and urea (to form competitive hydrogen bonds), respectively. The results showed that urea could block the inhibitory effect of SBI NPs on MRSA, so the combination of SBI NPs and MRSA was mainly through hydrogen bonds (Fig. 5E). Since 0.1% SDS is toxic to MRSA, the OD600 tends to 0. Meanwhile, SBI NPs have POD-like activity, so we evaluated the ability of iridium oxide nanoenzymes to mediate ROS production in bacterial microenvironments. As shown in Fig. 5F, the green fluorescence of MRSA treated with IrO_x NPs and SBI NPs increased compared to the control group, indicating an increase in intracellular ROS content. These results suggested that SBI NPs label MRSA in a hydrogen bond manner through the guanidinium peptide/betaine moiety and subsequently iridium oxide mediates ROS anti-MRSA activity.

Relieving lung bacterial infections

Lung diseases caused by microbial infections affect hundreds of millions of children and adults worldwide.[1] Herein, we constructed an acute lung infection model for evaluating the anti-bacterial activity of SBI NPs *in vivo* (Fig. 6A). Briefly, ICR mice (7 weeks) were infected with MRSA by a nasal drip and randomly divided into 3 groups of 5 mice each (set as day 1). On day 2, PBS, SBI NPs and vancomycin were administered intranasally to each mouse. On day 3, the lung tissues of the mice were removed and examined physiologically. Body weights were examined during the treatment, and the data demonstrated that no significant changes were found compared to the control group (Fig. 6B). As shown in Fig. 6C, it could be observed that the PBS group showed obvious pathological features such as redness and congestion, but the lung morphology of the SBI NPs and vancomycin groups returned to normal. In addition,

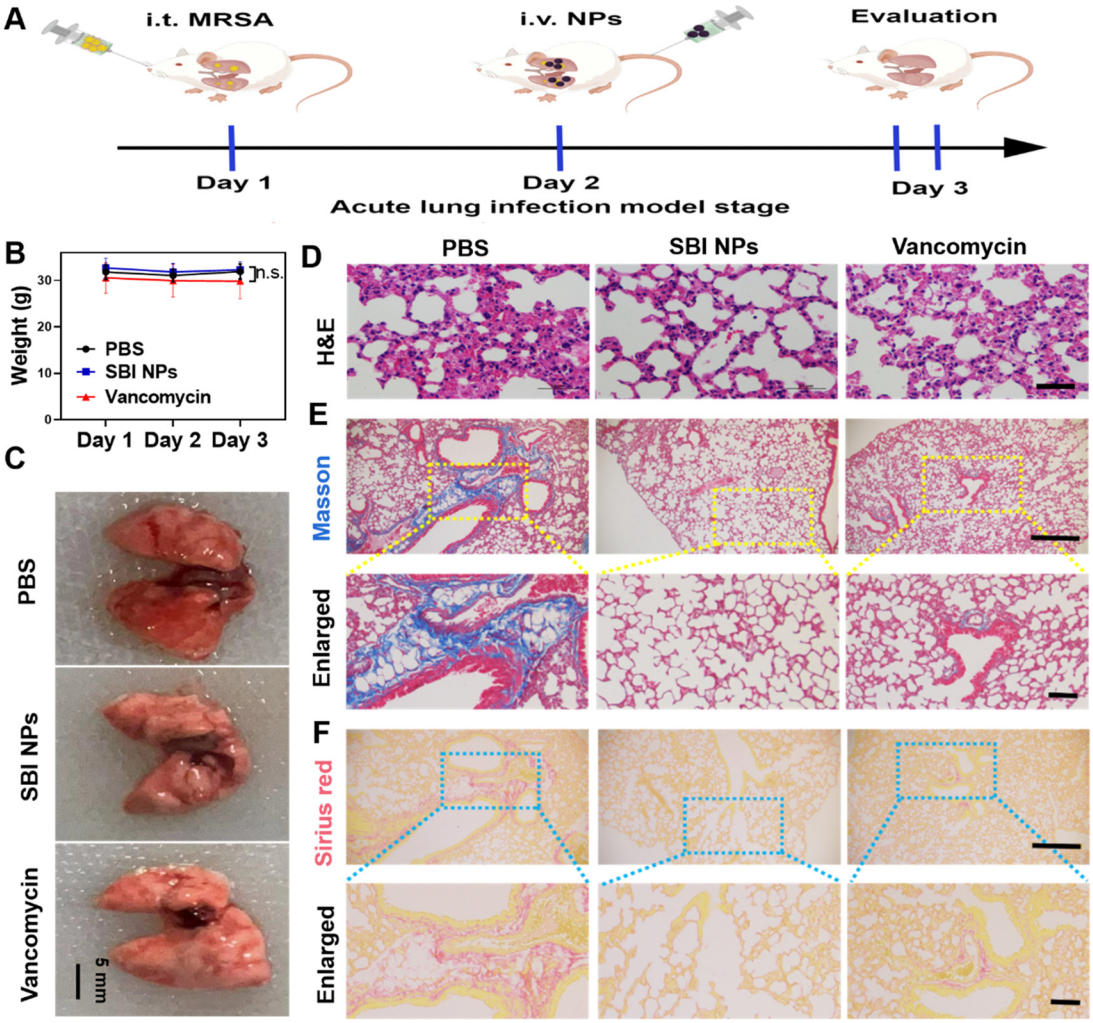

Fig. 6 Relieves lung bacterial infections. (A) Schematic illustration of the acute lung infection model and experimental procedures. (B) Body weight changes of mice during treatment (n = 5). (C) The appearance of lungs in various treatment groups. (D) H&E-stained histologic sections after the different treatments of lung tissues. Scale bar: 40 μm. Images of (E) Masson and (F) Sirius red staining for collagen deposition in lung tissues. Scale bar: 200 μm. *$p < 0.05$; **$p < 0.01$; ***$p < 0.001$ and n.s. not significant.

H&E staining was used to assess lung lesions. Compared to the control group, the SBI NPs and vancomycin groups had no edema as well as a reduction in the inflammatory response (Fig. 6D). Collagen deposition in the lung tissues was observed by using Masson and Sirius staining. The results demonstrated that the PBS group showed extensive lung damage and pulmonary fibrosis with incomplete alveolar expansion, indicating severe lung lesions. After treatment with vancomycin, the lung lesions were significantly better, but there was still a small amount of collagen deposition. In contrast, after treatment with SBI NPs, the lung tissue tended to be normal, with complete alveolar expansion and no fibrosis. These results indicated that SBI NPs had a significant improvement in the treatment of acute lung infections in mice (Fig. 6E and F). The above data confirmed that SBI NPs hold good anti-bacterial activity *in vivo*.

Diabetic wound healing

Generally, diabetic patients have difficulty in healing wounds and are more susceptible to bacterial infections. This is because the onset of diabetes affects blood circulation and prevents the growth of fresh granulation. This, combined with poor circulation, prevents the active ingredients of antibacterial drugs from being transported through the blood vessels to the wound to take effect, and the residue of sugar-rich blood in the wound increases the likelihood of bacterial infection. The combination of these factors can lead to increased infection, failure to heal the wound and further development of gangrene.[60] Therefore, we studied whether SBI NPs have the ability to heal diabetic wounds. As shown in Fig. 7A, we constructed a diabetic wound model as well as treatment measures. Briefly, ICR mice (7 weeks) were injected with STZ every other day and used to construct a diabetic mouse model of infection (fasting blood glucose values >11.1 mmol L^{-1}). During this period, changes in the body weight and blood glucose values were observed (Fig. 7B), compared to the beginning, and it was found that the mice exhibited significantly reduced body weight and showed symptoms of polyuria, polydipsia, and weight loss. After four injections of STZ, the

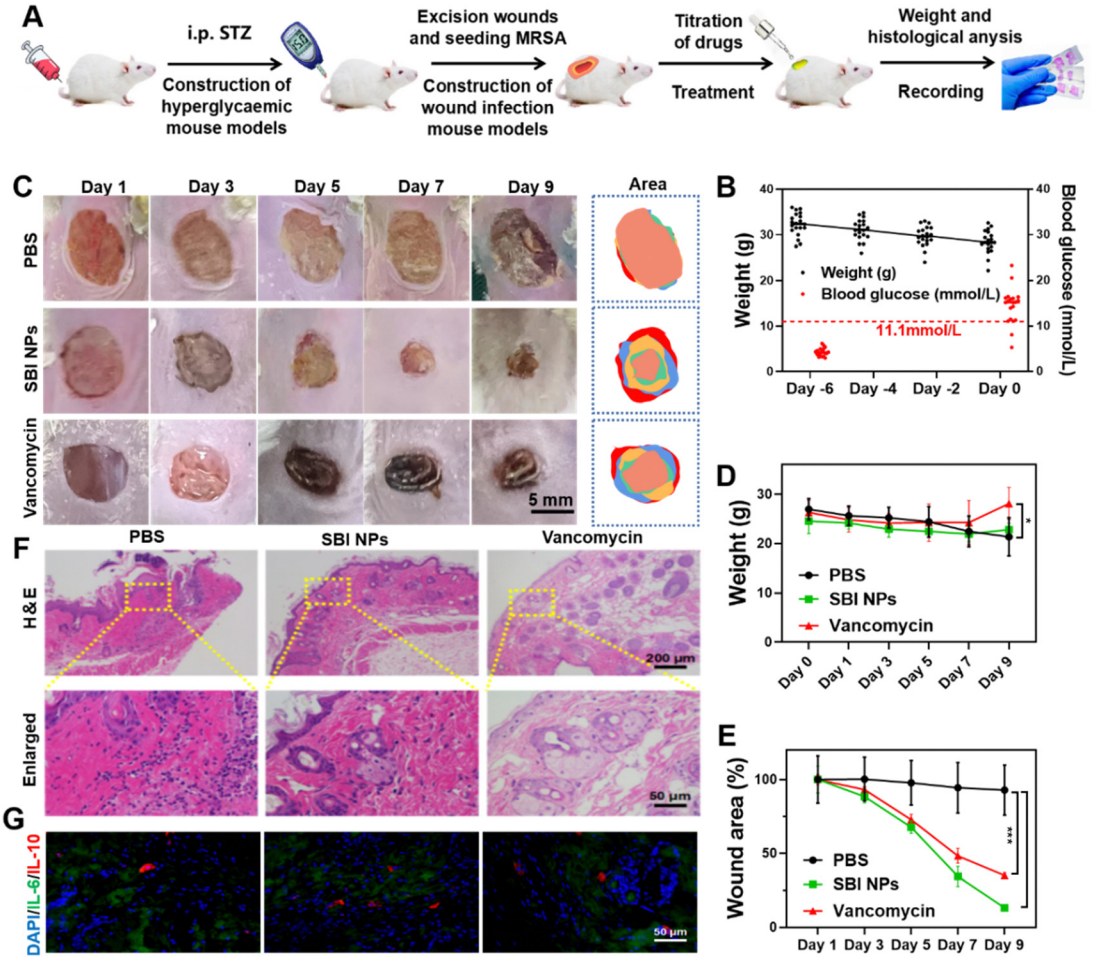

Fig. 7 Diabetic wound healing. (A) Schematic diagram of the experimental steps of the diabetic wound infection model. (B) Changes in the body weight and blood glucose of mice during the establishment of the diabetes model. (C) Macroscopic images of mice wounds during treatment. Scale: 5 mm. (D) Changes in the body weight of mice during treatment. (E) Quantitative analysis of wound area changes in each group of mice. (F) H&E stained sections of the skin tissue of mice in each group on day 9. Scale: 200 μm. (G) Immunofluorescence staining of IL-6 and IL-10 in skin wound tissue sections. Scale: 50 μm. $*p < 0.05$; $**p < 0.01$; $***p < 0.001$ and n.s. not significant.

percentage of hyperglycaemic mice was 90%. A circular wound (~8 mm in diameter) was then created on the back of the hyperglycaemic mice and MRSA was added dropwise to cause wound infection (set as Day 0). Macroscopic images of the wounds were analysed (Fig. 7C), and body weights were recorded (Fig. 7D) during the 9 days of treatment in the 3 groups of mice. The wound area of the SBI NPs group gradually closed and hair regrew (Fig. 7E). Subsequently, we performed H&E straining analysis of the three groups on day 9 (Fig. 7F), and the PBS group showed a large infiltration of inflammatory cells and severely damaged epidermal and dermal tissues. In stark contrast, the group of SBI NPs and vancomycin regenerated intact epithelial tissues at the damaged sites and the SBI NP group formed distinct hair follicle tissues. In addition, immunofluorescence staining of IL-6 and IL-10 demonstrated that the PBS group continued to stimulate the development of an inflammatory response, whereas the SBI NP and vancomycin groups were more likely to promote tissue repair (Fig. 7G). The above results suggested that SBI NPs have the ability to fight skin infections and promote diabetic wound healing.

Biosafety evaluation of SBI NPs

The biosafety of nanomaterials is an important indicator of whether they can be used for *in vivo* therapy. Therefore, we investigated the cytotoxicity of SBI NPs on mouse embryonic fibroblasts and human umbilical vein endothelial cells (Fig. 8A and B). The results showed that no significant cytotoxicity was detected at concentrations of SBI NPs ≤ 62.5 μg mL^{-1}. Even when the concentration was as high as 250 μg mL^{-1}, the two cells were still able to maintain the cell viability of about 80%. Next, blood safety was assessed by an erythrocytes-hemolysis assay. As shown in Fig. 8C, when the concentration of SBI NPs was increased from 15.625 to 250 μg mL^{-1}, the hemolysis rates were extremely low at less than 3%. Representative pictures of SBI NPs incubated with different concentrations of erythrocytes also supported the quantitative results. Furthermore, we injected high doses of SBI NPs (5 mg kg^{-1}) into healthy ICR mice and examined the effects on major organs. No significant changes were found in the H&E staining of important organs such as the heart, liver, spleen, lungs, and kidneys (Fig. 8D). These data indicated the good biosafety of SBI NPs in a certain concentration range.

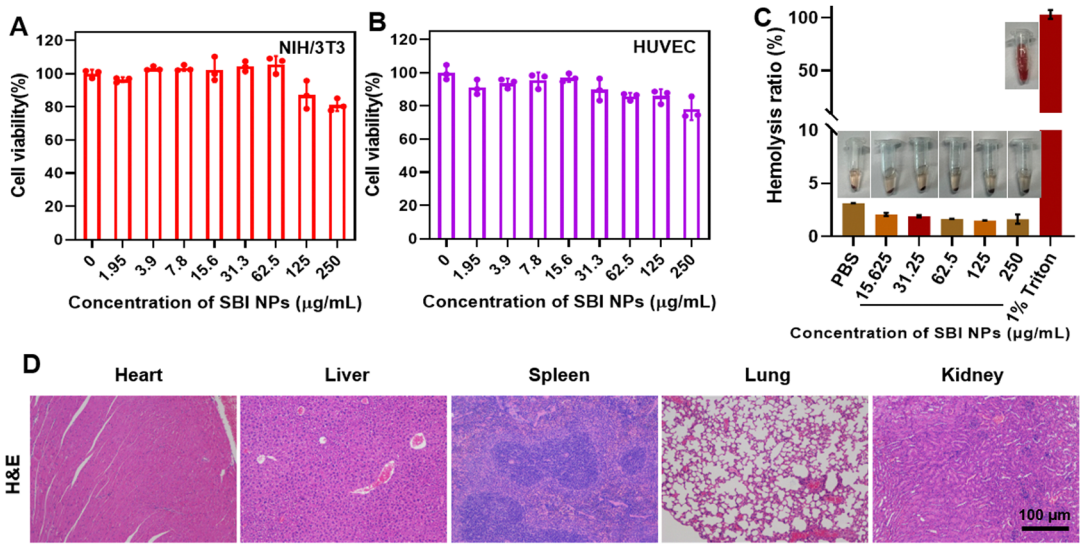

Fig. 8 Cytotoxicity of different concentrations of SBI NPs to (A) NIH/3T3 and (B) HUVECs. (C) Quantification of hemolysis of red blood cells at different concentrations of SBI NPs. (D) H&E staining of different organs of treatment mice.

3. Conclusions

In conclusion, we have successfully constructed a guanidinium peptide-modified iridium oxide nanozyme with good enzymatic catalytic activity and bacterial targeted binding ability. *In vitro* experiments showed that the modified guanidinium peptide could enhance the anti-biofilm activity of iridium oxide nanozymes and had better anti-biofilm activity than the clinical first-line drug *vancomycin*. Importantly, iridium oxide nanozymes functionalized with guanidinium peptides were able to effectively alleviate MRSA acute lung infection and effectively promote diabetic wound healing. Accordingly, functionalized iridium oxide nanozymes with guanidinium peptides are expected to be an effective antibiotic candidate in the post-antibiotic era.

Conflicts of interest

There are no conflicts to declare.

Acknowledgements

This research was funded by the PhD Start-up Fund of Guangdong Medical University (4SG23189G), Zhanjiang Marine Young Talent Innovation Project (2022E05013), the National Natural Science Foundation of China (Grant No. 21701034), the Science and Technology Program of Guangdong Province (Grant No. 2019B090905011), and the Science and Technology Program of Zhanjiang (Grant No. 2021A05044, 2021A05242).

References

1 W. Cookson, M. J. Cox and M. F. Moffatt, *Nat. Rev. Microbiol.*, 2018, **16**, 111–120.
2 C. Nathan, *Nat. Rev. Microbiol.*, 2020, **18**, 259–260.
3 H. Koo, R. N. Allan, R. P. Howlin, P. Stoodley and L. Hall-Stoodley, *Nat. Rev. Microbiol.*, 2017, **15**, 740–755.
4 L. S. J. Roope, R. D. Smith, K. B. Pouwels, J. Buchanan, L. Abel, P. Eibich, C. C. Butler, P. S. Tan, A. S. Walker, J. V. Robotham and S. Wordsworth, *Science*, 2019, **364**, eaau4679.
5 L. J. Shallcross, S. J. Howard, T. Fowler and S. C. Davies, *Philos. Trans. R. Soc. London, Ser. B*, 2015, **370**, 20140082.
6 C. Willyard, *Nature*, 2017, **543**, 15.
7 S. George, F. F. Muhaj, C. D. Nguyen and S. K. Tyring, *J. Am. Acad. Dermatol.*, 2022, **86**, 1189–1204.
8 P. C. M. Williams, D. Isaacs and J. A. Berkley, *Lancet Infect. Dis.*, 2018, **18**, e33–e44.
9 F. Micoli, F. Bagnoli, R. Rappuoli and D. Serruto, *Nat. Rev. Microbiol.*, 2021, **19**, 287–302.
10 D. I. Andersson, D. Hughes and J. Z. Kubicek-Sutherland, *Drug Resistance Updates*, 2016, **26**, 43–57.
11 Q. Yu and J. B. Fein, *Environ. Sci. Technol.*, 2016, **50**, 5498–5505.
12 J. He, M. Hong, W. Xie, Z. Chen, D. Chen and S. Xie, *J. Controlled Release*, 2022, **351**, 301–323.
13 P. J. F. Henderson, C. Maher, L. D. H. Elbourne, B. A. Eijkelkamp, I. T. Paulsen and K. A. Hassan, *Chem. Rev.*, 2021, **121**, 5417–5478.
14 I. Karaiskos and H. Giamarellou, *Expert Opin. Pharmacother.*, 2014, **15**, 1351–1370.
15 Z. Chen, H. Ji, C. Liu, W. Bing, Z. Wang and X. G. Qu, *Angew. Chem.*, 2016, **55**, 10732–10736.
16 Y. Gao, J. Wang, M. Chai, X. Li, Y. Deng, Q. Jin and J. Ji, *ACS Nano*, 2020, **14**, 5686–5699.
17 O. Ciofu, C. Moser, P. Jensen and N. Høiby, *Nat. Rev. Microbiol.*, 2022, **20**, 621–635.
18 L. Hall-Stoodley, J. W. Costerton and P. Stoodley, *Nat. Rev. Microbiol.*, 2004, **2**, 95–108.
19 J. W. Costerton, P. S. Stewart and E. P. Greenberg, *Science*, 1999, **284**, 1318–1322.

20 D. Davies, *Nat. Rev. Drug Discovery*, 2003, **2**, 114–122.
21 H. R. Jia, Y. X. Zhu, Q. Y. Duan and F. G. Wu, *Chem. Soc. Rev.*, 2021, **50**, 6240–6277.
22 S. Guo, Q. Huang, Y. Chen, J. Wei, J. Zheng, L. Wang, Y. Wang and R. Wang, *Angew. Chem.*, 2021, **60**, 618–623.
23 W. Jiang, M. Zhou, Z. Cong, J. Xie, W. Zhang, S. Chen, J. Zou, Z. Ji, N. Shao, X. Chen, M. Li and R. Liu, *Angew. Chem.*, 2022, **61**, e202200778.
24 J. Wang, X. Y. Chen, Y. Zhao, Y. Yang, W. Wang, C. Wu, B. Yang, Z. Zhang, L. Zhang, Y. Liu, X. Du, W. Li, L. Qiu, P. Jiang, X. Z. Mou and Y. Q. Li, *ACS Nano*, 2019, **13**, 11686–11697.
25 Y. Liu, L. Shi, L. Su, H. C. van der Mei, P. C. Jutte, Y. Ren and H. J. Busscher, *Chem. Soc. Rev.*, 2019, **48**, 428–446.
26 D. Hu, Y. Deng, F. Jia, Q. Jin and J. Ji, *ACS Nano*, 2020, **14**, 347–359.
27 Q. Deng, P. Sun, L. Zhang, Z. Liu, H. Wang, J. Ren and X. Qu, *Adv. Funct. Mater.*, 2019, **29**, 1903018.
28 J. Xie, M. Zhou, Y. Qian, Z. Cong, S. Chen, W. Zhang, W. Jiang, C. Dai, N. Shao, Z. Ji, J. Zou, X. Xiao, L. Liu, M. Chen, J. Li and R. Liu, *Nat. Commun.*, 2021, **12**, 5898.
29 W. Ji, C. Yuan, P. Chakraborty, P. Makam, S. Bera, S. Rencus-Lazar, J. Li, X. Yan and E. Gazit, *ACS Nano*, 2020, **14**, 7181–7190.
30 K. M. O'Connell, J. T. Hodgkinson, H. F. Sore, M. Welch, G. P. Salmond and D. R. Spring, *Angew. Chem.*, 2013, **52**, 10706–10733.
31 J. Wang, C. Lu, Y. Shi, X. Feng, B. Wu, G. Zhou, G. Quan, X. Pan, J. Cai and C. Wu, *ACS Appl. Mater. Interfaces*, 2020, **12**, 18363–18374.
32 Y. Huang, Q. Gao, X. Li, Y. Gao, H. Han, Q. Jin, K. Yao and J. Ji, *Nano Res.*, 2020, **13**, 2340–2350.
33 P. Sangtanoo, P. Srimongkol, T. Saisavoey, O. Reamtong and A. Karnchanatat, *Food Funct.*, 2020, **11**, 552–560.
34 J. J. Yang, X. D. Zhang, Y. H. Ma, G. Gao, X. K. Chen, H. R. Jia, Y. H. Li, Z. Chen and F. G. Wu, *ACS Appl. Mater. Interfaces*, 2016, **8**, 32170–32181.
35 B. Yang, Y. Chen and J. Shi, *Adv. Mater.*, 2019, **31**, e1901778.
36 Y. Huang, J. Ren and X. G. Qu, *Chem. Rev.*, 2019, **119**, 4357–4412.
37 K. Dong, E. Ju, N. Gao, Z. Z. Wang, J. S. Ren and X. G. Qu, *Chem. Commun.*, 2016, **18**, 5312–5315.
38 F. F. Cao, L. Zhang, H. Wang, Y. W. You, Y. Wang, N. Gao, J. S. Ren and X. G. Qu, *Angew. Chem.*, 2019, **58**, 16236–16242.
39 H. Qiu, F. Pu, Z. W. Liu, Q. Q. Deng, P. P. Sun, J. S. Ren and X. G. Qu, *Small*, 2019, **15**, e1902522.
40 T. T. Cui, S. Wu, Y. H. Sun, J. S. Ren and X. G. Qu, *Nano Lett.*, 2020, **20**, 7350–7358.
41 X. Zhu, Y. Gong, Y. Liu, C. Yang, S. Wu, G. Yuan, X. Guo, J. Liu and X. Qin, *Biomaterials*, 2020, **242**, 119923.
42 H. Wang, K. Wan and X. Shi, *Adv. Mater.*, 2019, **31**, e1805368.
43 M. Li, Q. Liu, Z. J. Jia, X. C. Xu, Y. Y. Shi, Y. Cheng and Y. F. Zheng, *J. Mater. Chem. B*, 2015, **3**, 8796–8805.
44 X. Li, K. Z. Ahmad, J. He, H. X. Li, X. Wang, Z. J. Feng, X. S. Wang, G. X. Shen and X. T. Ding, *J. Mater. Chem. B*, 2021, **9**, 9839–9851.
45 L. Z. Gao, J. Zhuang, L. Nie, J. B. Zhang, Y. Zhang, N. Gu, T. H. Wang, J. Feng, D. L. Yang, S. Perrett and X. Y. Yan, *Nat. Nanotechnol.*, 2007, **2**(2007), 577–583.
46 K. N. Zhu, S. Y. Qian, H. W. Guo, Q. Y. Wang, X. Y. Chu, X. Y. Wang, S. Lu, Y. Peng, Y. S. Guo, Z. Q. Zhu, T. Y. Qin, B. Liu, Y. W. Yang and B. L. Wang, *ACS Nano*, 2022, **16**, 11136–11151.
47 H. R. Zhang, W. Y. Jiang, Y. Peng, J. Yang, X. Y. Chu, Z. Y. Long, R. L. Li, Q. W. Liang, H. Suo, S. T. Wang, M. Yang, J. Qi, D. Ding, Y. W. Yang and B. L. Wang, *Biomaterials*, 2022, **286**, 121577.
48 Z. Q. Zhu, L. Wang, Y. Peng, X. Y. Chu, L. Y. Zhou, Y. Y. Jin, H. W. Guo, Q. Gao, J. H. Yang, X. Y. Wang, Z. Y. Long, Y. F. Ge, S. Lu and B. L. Wang, *Adv. Funct. Mater.*, 2022, **32**, 2201875.
49 X. Zhang, Z. Zhang, Q. Shu, C. Xu, Q. Zheng, Z. Guo, C. Wang, Z. Hao, X. Liu, G. Wang, W. Yan, H. Chen and C. Lu, *Adv. Funct. Mater.*, 2021, **31**, 2008720.
50 A. Lin, Y. Liu, X. Zhu, X. Chen, J. Liu, Y. Zhou, X. Qin and J. Liu, *ACS Nano*, 2019, **13**, 13965–13984.
51 Y. Huang, Y. Liu, S. Shah, D. Kim, A. Simon-Soro, T. Ito, M. Hajfathalian, Y. Li, J. C. Hsu, L. M. Nieves, F. Alawi, P. C. Naha, D. P. Cormode and H. Koo, *Biomaterials*, 2021, **268**, 120581.
52 G. Guo, H. Zhang, H. Shen, C. Zhu, R. He, J. Tang, Y. Wang, X. Jiang, J. Wang, W. Bu and X. Zhang, *ACS Nano*, 2020, **14**, 13391–13405.
53 A. P. Castano, T. N. Demidova and M. R. Hamblin, *Photodiagn. Photodyn. Ther.*, 2005, **2**, 1–23.
54 F. Gao, T. Shao, Y. Yu, Y. Xiong and L. Yang, *Nat. Commun.*, 2021, **12**, 745.
55 W. Zhen, Y. Liu, W. Wang, M. Zhang, W. Hu, X. Jia, C. Wang and X. Jiang, *Angew. Chem., Int. Ed.*, 2020, **59**, 9491–9497.
56 W. Zhen, Y. Liu, M. Zhang, W. Hu, W. Wang, X. Jia and X. Jiang, *Adv. Funct. Mater.*, 2020, **30**, 2002274.
57 L. A. Fontana, V. H. Rigolin, C. B. Braga, C. Ornelas and J. D. Megiatto, *Chem. Commun.*, 2021, **57**, 7398–7401.
58 D. Sun, X. Pang, Y. Cheng, J. Ming, S. Xiang, C. Zhang, P. Lv, C. Chu, X. Chen, G. Liu and N. Zheng, *ACS Nano*, 2020, **14**, 2063–2076.
59 X. Ma, L. Wang, P. Wang, Z. Liu, J. Hao, J. Wu, G. Chu, M. Huang, L. O. Mair, C. Huang, T. Xu, T. Ying, X. Tang, Y. Chen, X. Cai and Y. Zheng, *Chem. Eng. J.*, 2022, **431**, 133971.
60 S. Matoori, A. Veves and D. J. Mooney, *Sci. Transl. Med.*, 2021, **13**, eabe4839.